Processing and characterization of an electrodeposited nanocrystalline Co–Fe–Ni–Zn multi-principal element alloy film

Péter Nagy [a], László Péter [b], Zsolt Czigány [c], Nguyen Quang Chinh [a], Jenő Gubicza [a,*]

[a] Department of Materials Physics, Eötvös Loránd University, P.O.B. 32, H–1518 Budapest, Hungary
[b] Wigner Research Centre for Physics, P.O.B. 49, H–1525 Budapest, Hungary
[c] Institute for Technical Physics and Materials Science, Centre for Energy Research, Konkoly-Thege M. út 29-33, H-1121 Budapest, Hungary

ABSTRACT

A Co—Fe—Ni—Zn multi-principal element alloy (MPEA) film with the thickness of about 2.5 μm is processed by electrodeposition. The layer has a nanocrystalline microstructure with the grain size of about 12 nm as determined by transmission electron microscopy. The structure of the majority of the film is face-centered cubic (fcc); however, body-centered cubic (bcc) and amorphous phases with small fractions are also detected. The average hardness and elastic modulus of the coating are 9.2 and 197 GPa, respectively, as determined by nanoindentation. The hardness value is superior compared to other fcc MPEA layers processed by different deposition methods. The enhanced hardness can be attributed to the strengthening effect of the very small grain size and the presence of nanocrystalline bcc and amorphous minority phases. This study demonstrates the ability of electrodeposition for producing hard MPEA layers with the desired composition.

1. Introduction

One of the most dynamically developing fields of materials science focuses on studying equiatomic or near-equiatomic materials with three or more elements [1]. In the case of such materials, there are no solvents and solutes; therefore, they are frequently called as multi-principal element alloys (MPEAs) or compositionally complex alloys (CCAs) [1,2]. These materials also include high-entropy alloys (HEAs), which refer to a specific subset of materials where the number of principal elements is five or higher with an atomic concentration between 5 % to 35 % [3]. HEAs usually display a single-phase microstructure due to the stabilizing effect of the high entropy caused by the large number of principle elements with the same or similar concentrations [3]. MPEAs have been vastly investigated in the recent years due to their outstanding mechanical and physical properties. For instance, excellent oxidation and wear resistance [4], exceptional strength even at high-temperatures [5], and for some compositions, a combination of high strength and good ductility [6] were demonstrated. Owing to the wide range of possible compositions, the properties of MPEAs could be tailored for multiple purposes. For instance, mechanical applications due to the remarkable hardness, high tensile strength and good ductility [7,8] can be combined with medical applications owing to the

antibacterial properties, corrosion resistance and biocompatibility [9,10].

MPEAs can be manufactured with a wide range of techniques. For example, bulk MPEAs were fabricated via mechanical alloying [11] and arc-melting [12], and an additional grain refinement was performed using high-pressure torsion [13] in order to get a nanocrystalline microstructure. MPEA materials are also produced in the form of thin films since they attract significant scientific interest due to their exceptional properties. In the recent years, ion beam sputtering was utilized to produce a FeCrSiNb layer with a thickness of 1.5 μm, and this film exhibited a high hardness and an outstanding corrosion resistance [14]. In another study, $Fe_{26.7}M_{26.7}Ga_{15.6}Mn_{20}Si_{11}$ coatings (M: Co or Ni) having the thickness of about 80 nm was synthesized via thermal evaporation for magnetoresistance applications [15]. Lately, some works focused on combinatorial MPEA films in which the concentrations of the constituent elements change laterally, therefore many different compositions can be studied in a single sample [16–20]. For instance, the corrosion properties of a combinatorial sample of $Al_x(CoCrFeNi)_{100-x}$ produced by radiofrequency magnetron sputtering were investigated [16]. In this case, the layer thickness was 240 nm, and the study showed that the corrosion resistance of the thin film MPEA is superior to the bulk counterpart. It was also found that with the increase of Al concentration,

* Corresponding author.
  E-mail address: jeno.gubicza@ttk.elte.hu (J. Gubicza).

the resistance of the layer to corrosion decreased. Recently, in a series of studies CoCrFeNi combinatorial films with a thickness of approximately 1 μm were investigated in detail [17–20]. These samples were produced by a novel PVD method, namely multiple beam sputtering. The phase composition, the crystallite size and the density of lattice defects (e.g., dislocations) were investigated as a function of the chemical composition [17–19], and a novel machine learning-based method was used for construction maps of the microstructure [20]. In addition, the hardness and the elastic modulus versus the chemical composition in the Co—Cr—Fe—Ni MPEA system were determined by nanoindentation [18,19].

It should be noted that PVD techniques are able to produce very thin films on flat surface of a substrate. Therefore, if a workpiece with complicated shape is intended to cover with an MPEA layer, another method must be used. For instance, electroplating is a conventional technique which is able to deposit thick films on surfaces with complicated shapes. The first attempts of MPEA electroplating were based on the application of non-aqueous solvents [21–28], hence taking advantage of the possibility of the reduction of a greater variety of meal ions than from aqueous solutions. Beside transition metals that are commonly available by aqueous electroplating, rare-earth metals were also among the components deposited [22–24]. In many of these studies, the concentration of the precursor metal salts was in the 1–100 mM range. The deposition of at least some of the components took place at the diffusion-limited current density, which offers an opportunity to tune the deposit composition directly with the bath concentrations, independently of the codeposition mode of the metals. When pulse plating was applied [26], the frequency of the pulses much exceeded the threshold where capacitive distortion is expected to occur [29,30].

Attempts with aqueous electrodeposition to produce HEAs appeared much after the nonaqueous systems [31–35] due to the limitations of the components and the difficulties of the system optimization because of the water decomposition. Apart from 4d metals, the alloys contained in some cases P and Bi [31], Al [34] and Mo and W [35]. Some deposits were reported to be inhomogeneous at the micrometer scale [35], but pulse-plated alloys proved to be homogeneous at the resolution scale of the EDS maps [33]. In most cases, magnetic properties were in the focus of these studies. Templated electrodeposition of HEA nanowires was demonstrated with aqueous baths [36], leading to a homogeneous component distribution along the nanowire as a result of the optimized pulse plating approach.

Oxygen content of the MPEAs deposited from nonaqueous media was not even mentioned in these studies. Nevertheless, the oxygen K-line was sometimes indicated in the EDX spectra [21–24], and its height was often comparable to [25,34] or even much larger [27] than that of the metals. This indicates a substantial degree of oxidation (or incomplete reduction of the metal ions). For the sake of completeness, it has to be mentioned that electroreduction of compacted metal oxide pellets in molten salts also became a prominent technique to produce MPEAs [37–43]. Although the resulting metals are porous, this technique is feasible to produce alloys with metal components that are not completely reducible from dissolved ions.

Although several attempts had already been made to produce MPEA coatings by electroplating as discussed above, there are numerous many-component MPEA systems which have not been produced successfully by electrodeposition. An MPEA alloy layer composed of Co—Fe—Ni—Zn is expected to exhibit various advantageous features. First, all components are inexpensive and relatively non-toxic materials. Secondly, Zn together with the iron group metals can be deposited from aqueous solutions, which points toward the relatively easy adaptation of the deposition of such an alloy into existing technologies. Thirdly, the mutual codeposition characteristics of any pairs of this quadruplet are well described in the literature, which offers a sufficient guideline for the plating procedure of the quaternary alloy.

In this study, a Co—Fe—Ni—Zn MPEA is processed by pulse electroplating for the first time, yielding a coating with the thickness of

about 2.5 μm. The microstructure and the hardness were characterized in detail and compared with the features of other electrodeposited MPEAs.

2. Experimental details

2.1. Sample preparation

A Co—Fe—Ni—Zn MPEA layer was processed by electrodeposition. All chemicals used for the solution preparation were of analytical grade. The concentrations of the solution components are summarized in Table 1. Metal salts were the precursor compounds of the electrodeposition, boric acid was a buffering agent, saccharin is a commonly used stress reliever for nickel-based electrodeposited coatings, sodium dodecylsulfate is a wetting agent, while ascorbic acid is an essential antioxidant to suppress the spontaneous oxidation of the Fe^{2+} ions. Solutions were prepared freshly every day from stock solutions of all metal salts except for the ion-containing compound that was added to the solution as solid and then dissolved, hence preventing the oxidation upon storage. Ultrapure water supplied from an ELGA Purelab Option 7 purifier was used in every experiment. The pH of the bath was 3.2 ± 0.1 (measured at room temperature). There was no appreciable change in pH observed after the alloy plating procedure.

The schematic view of the beaker-type electrochemical cell is shown in Fig. 1. The Teflon® cathode holder was assembled and then immersed into the pre-heated solution. Tantalum was used as cathode because of two reasons: (i) Ta is very stable in aqueous solutions due to its intact protecting oxide layer, which also serves as a crystallographically neutral surface that provides no preferred orientation of the deposit; (ii) The XRD lines of the Ta substrate are far from the expected diffraction lines of the deposits, hence providing an overlap-free background for the structural analysis. The anode was a nickel foil cylindrically arranged along the internal wall of the beaker. The total anode surface area was more than 100 times larger than that of the cathode. The cylindrical configuration ensured that no residue of the anode can fall onto the cathode even if the anode disintegrates due to the dissolution. The current distribution was sufficiently even along the cathode surface, as it will be evidenced from the subsequent composition map. All experiments were performed at 55 ± 0.2 °C, which was stabilized by immersing the entire beaker into a thermostat. The choice of the elevated temperature is rationalized with the result of the preliminary experiments, showing that a morphologically and compositionally heterogeneous deposit is obtained at room temperature. After the deposition, the entire cathode holder could be easily removed from the cell, and the deposit was immediately rinsed with ultrapure water several times then with ethanol to prevent the oxidation of either the deposit or the solvent residues.

Electrodeposition was performed with pulse plating and with fixed on- and off-times (0.06 s and 0.7 s, respectively), with 28 mA cm^{-2} on-time current density. The sample was prepared by applying 6000 pulses (overall accumulated on-time: 360 s). The choice of the pulse plating parameters was based on the observation that D.C. plating leads to a

Table 1
The concentrations of the initial chemicals in the solution utilized in the electrodeposition.

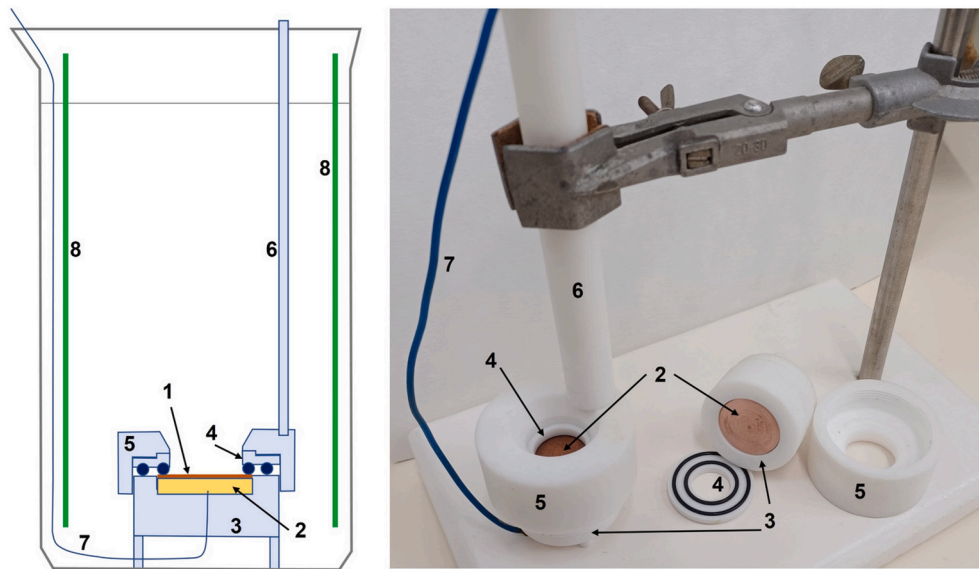| Name of the chemical [formula of the compound used for bath preparation]	Concentration [mol/l]
Nickel chloride [$NiCl_2 \cdot 6H_2O$]	0.1594
Cobalt chloride [$CoCl_2 \cdot 6H_2O$]	0.0548
Iron(II) ammonium sulfate [$(NH_4)_2Fe(SO_4)_2 \cdot 6H_2O$]	0.1419
Zinc sulfate [$ZnSO_4 \cdot 6H_2O$]	0.0130
Boric acid [H_3BO_3]	0.2500
Saccharin [$C_7H_5NO_3S$]	0.0273
Ascorbic acid [$C_6H_8O_6$]	0.0057
Sodium dodecylsulfate [$CH_3(CH_2)_{11}OSO_3Na$]	0.0014

Fig. 1. Schematic cross-sectional view of the electrochemical cell used (left) with the photo of both the fully assembled cathode and some of its dismounted parts (right). 1: Tantalum foil cathode; 2: Copper contact plate; 3: Bottom body of the electrode holder; 4: Internal joint with two O-rings to provide sealing; 5: Top part of the electrode holder; 6: Handle of the immersion cathode; 7: Electric lead to the cathode (sealed outside of the electrode holder); 8: Cylindrical nickel anode.

graded composition at the early phase of the process [44–46], but pulse plating with a duty cycle less than about 0.2 ensures a compositionally homogeneous alloy along the growth direction [47,48]. An EF453 potentiostat/galvanostat was used as the power source.

2.2. Structural studies

The surface morphology of the electrodeposited layer was studied by scanning electron microscopy (SEM) using a TESCAN MIRA3 microscope. The same SEM facility was applied in mapping the chemical composition of the whole coating by energy-dispersive X-ray spectroscopy (EDS).

The phase composition of the layer was characterized by X-ray diffraction (XRD). A Smartlab X-ray diffractometer (manufacturer: Rigaku, Japan) with Bragg–Brentano geometry and CuKα radiation (wavelength: $\lambda = 0.15418$ nm) was utilized. The XRD pattern was measured in scattering angles between 40 and 100° with a step size of 0.02°.

The cross-sectional microstructure of the layer was investigated by transmission electron microscopy (TEM). A TEM lamella was prepared by focused ion beam (FIB) technique using Ga^+ ions in a Thermo Scientific Scios 2 Dual Beam equipment Thermo Fisher Scientific, Waltham, MA, USA). The microstructure (and composition) was studied by transmission electron microscopy (TEM) including high resolution TEM (HR-TEM) and selected area electron diffraction (SAED) using a C_S corrected Thermo Fisher Themis TEM (Thermo Fisher Scientific, Waltham, MA, USA) equipped with four EDS detectors in Super-X geometry. Analysis was performed at 200 kV accelerating voltage with point resolution of 0.08 nm. High angle annular dark field (HAADF) images and EDS elemental maps were recorded in scanning transmission electron microscopy (STEM) mode.

2.3. Hardness test

The hardness and the elastic modulus of the sample were investigated by indentation measurements using a UMIS (manufacturer: CSIRO, Australia) nanoindentation device with Vickers type indenter. Considering the small sample thickness of about 3 μm, a low maximum load of 10 mN was applied in order to maintain the maximum penetration depth below ~300 nm. A series of 100 indentations along a line

with neighbor spacing of 20 μm was recorded on the sample. The indentation rate was 0.25 mN/s. The hardness and the elastic modulus were determined by the method of Oliver and Pharr [49].

3. Results and discussion

3.1. Analysis of the chemical composition

Fig. 2a shows a lateral overview of the film as obtained by SEM. The diameter of the coated area was about 16 mm. The light gray spots on the freshly prepared sample were due to the discoloration during the uneven drying after the final rinsing process and could not be identified as either morphologically or compositionally distinct areas in larger resolution images. The highly magnified SEM image in Fig. 2b reveals that the coating surface has a cauliflower-like morphology consisting of nanocrystalline grains as shown in the inset. A more detailed analysis of the grain structure on the cross section of the layer was performed by TEM and the results will be presented later in this section.

The elemental maps obtained for the four constituents of the studied MPEA by SEM-EDS can be seen in Fig. 3. A detailed study of the microstructure and hardness was performed only in the middle part of the film which exhibited a relatively homogeneous chemical composition. Namely, in a circular area at the film center with a diameter of 2 mm the chemical composition was 32 % Co, 27 % Fe, 21 % Ni and 20 % Zn (at.%) as determined by SEM-EDS. The uncertainty of the concentration values was about 1 at.%.

The complexity of the bath composition optimization is shown in Table 2. While the studied ternary system is the prominent example for the anomalous codeposition mode in metal plating [50–53], the anomality parameter shows even the normal codeposition for one metal pair. When the anomality parameter as calculated with the $(x_A/x_B)/(c_A/c_B)$ ratio is larger than one for a metal pair in which A is the less noble component in accord with the standard potentials, the codeposition mode is anomalous. It is straightforward from Table 2 that the Fe—Co pair follows the normal codeposition mode, while the codeposition of all other pairs is anomalous to various extent. The wide range of the anomality parameter leads to that the bath optimization for the near-equimolar deposit composition can be carried out with sequential approximations only because the change of just one single bath composition variable has a hardly predictable impact on the overall composition
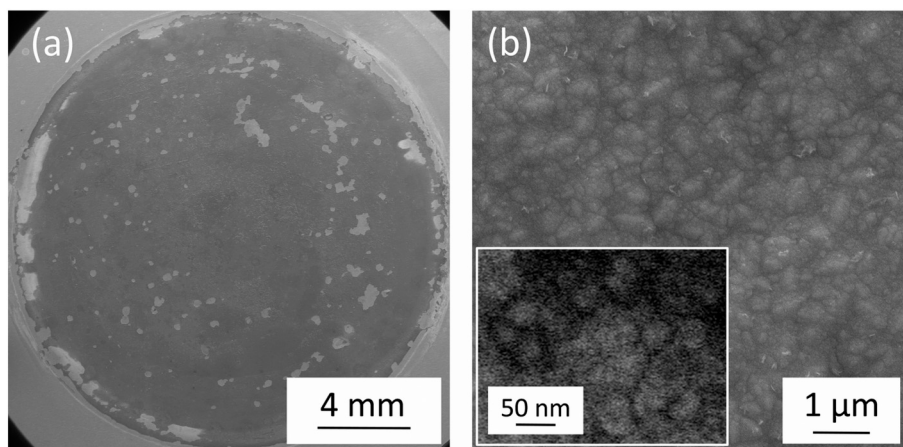
Fig. 2. (a) SEM overview of the full deposited disk. (b) A SEM image with higher magnification showing the cauliflower-like surface morphology. The highly magnified inset in (b) shows grains on the surface.
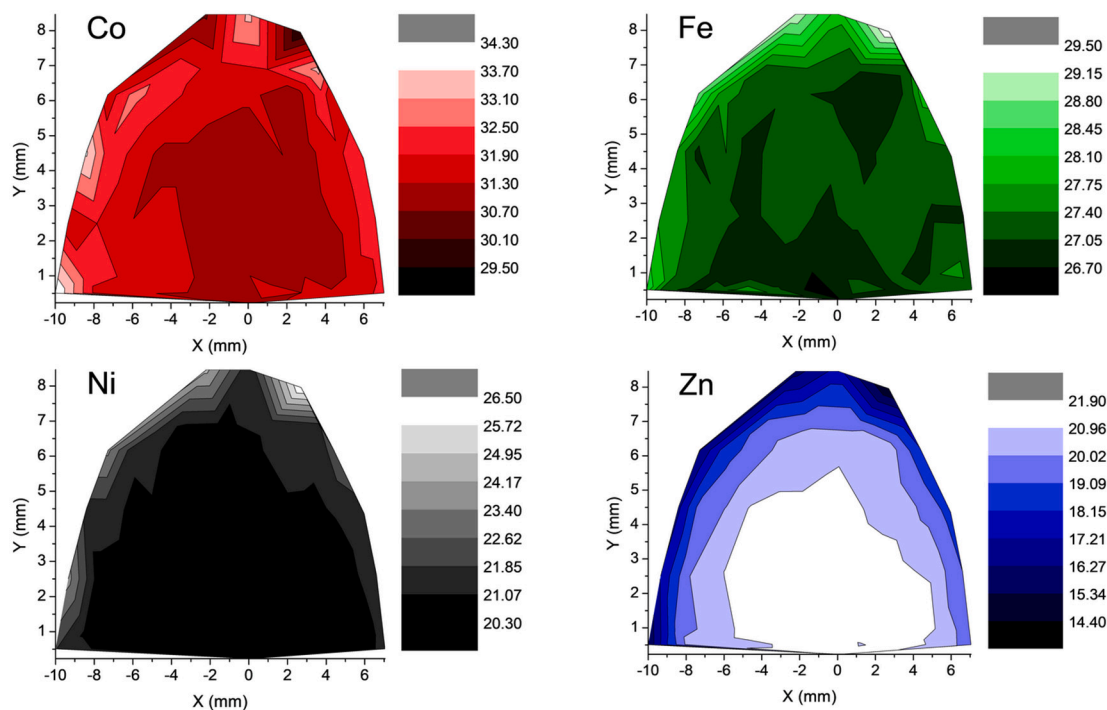

Fig. 3. Co, Fe, Ni and Zn elemental maps for one-half of the Co–Fe–Ni–Zn film as obtained by SEM-EDS. The values at the colour code indicate the concentrations in at.%.

Table 2
The $(x_A/x_B)/(c_A/c_B)$ parameters indicating the normal or anomalous nature of the codeposition for each metal pair. x: mole fraction in the deposit; c: concentration of the precursor compound in the bath; A and B are the components of the deposit. Components are listed in the order of their thermodynamic nobility.

		B		
		Fe	Co	Ni
A	Zn	8.09	2.77	11.6
	Fe	–	0.33	1.44
	Co	–	–	4.43

of the deposit.

The current efficiency was calculated on the basis of Faraday's law by using Eq. 1:

$$\frac{I_{ON}t_{ON}N\eta}{zF}\frac{M}{\rho} = Ad \tag{1}$$

where η is the current efficiency, I_{ON} is the on-time current, t_{ON} is the on-time, N is the number of current pulses applied to get the sample, z is the charge of the precursor ions in electron charge unit, F is the Faraday constant, M is the mean molar weight of the alloy, ρ is the density of the alloy, A is the surface area of the deposit as measured from Fig. 2a, and d is the mean thickness obtained from the cross-sectional cut used for TEM studies. The current efficiency hence estimated is 72 ± 2 %.

3.2. Structural studies

The XRD pattern taken on the center part of the film is shown in Fig. 4a. It is revealed that the main phase in the Co—Fe—Ni—Zn film has
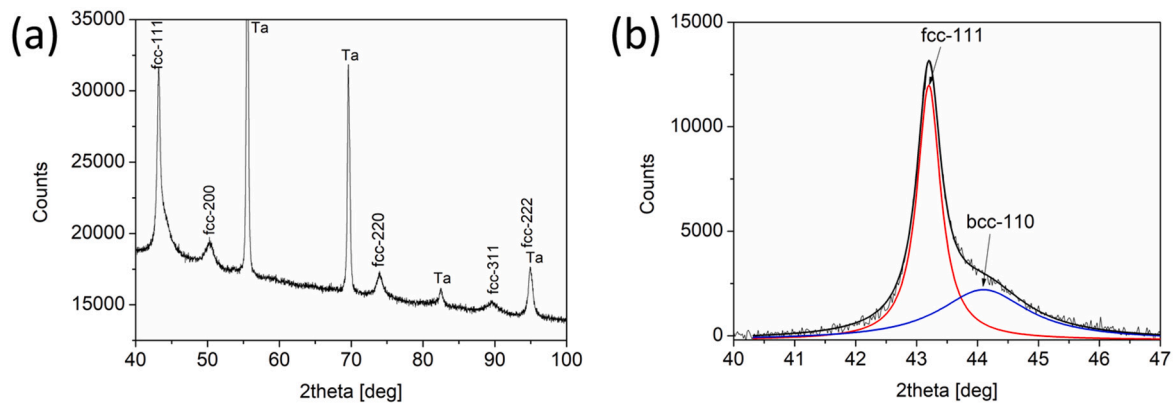
Fig. 4. (a) XRD pattern obtained in the center part of the Co—Fe—Ni—Zn film disk. (b) Magnified view of the first XRD peak after background subtraction, showing the fitting of the double peak with the sum of two Lorentzian functions.

an fcc structure. Additionally, the peaks of the Ta substrate also appeared in the diffractogram. The fcc reflection 111 has a shoulder at its right side, suggesting that this peak overlaps with another reflection located at a higher angle and having a lower intensity as shown in Fig. 4b. TEM diffraction study will reveal that this peak corresponds to a 110 reflection of a minor bcc phase (see later in this section). For further analysis, the positions, areas and breadths of the two overlapping peaks were determined by fitting a sum of two Lorentzian functions to the measured profile.

Fig. 5a shows the Nelson–Riley plot [54] for the determination of the lattice constant of the main fcc phase. In this plot, the lattice constant values determined from the positions of the XRD peaks are plotted as a function of $cos\theta \cdot (ctg\theta + cos\theta/\theta)$ where θ is the Bragg angle. The lattice constant of the fcc phase was determined from the intersection of the vertical axis and the straight line fitted to the data points in the Nelson–Riley plot as shown in Fig. 5a and the value of 0.3620 ± 0.0002 nm was obtained. The crystallite size of the main fcc phase can be estimated as the reciprocal of the FWHM of the first 111 peak which gives about 20 nm. This method is called as the Scherrer method [55]. It is worth noting that the Scherrer analysis usually underestimates the crystallite size since (i) it gives the average length of the columns obtained by cutting the crystallites perpendicular to the reflecting planes, which is usually smaller than the diameter of crystallites; and (ii) the lattice strain also contributes to the FWHM of the first diffraction peak; i.e., the measured broadening is higher than that caused by the crystallite size solely [55]. Nevertheless, the crystallite size determined by the Scherrer method is in a reasonable agreement with the grain size suggested by the inset in Fig. 2b.
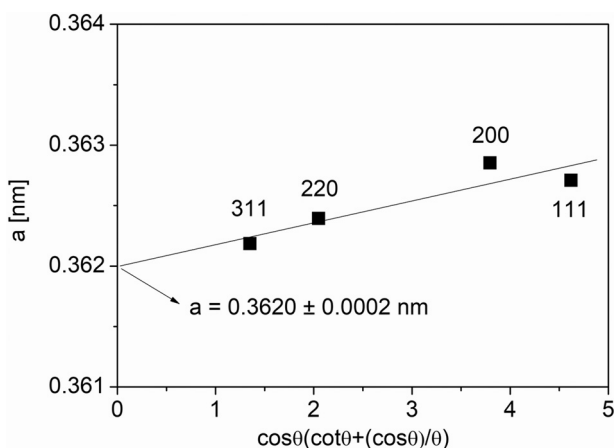
Fig. 6 shows a cross-sectional view of the Co—Fe—Ni—Zn film as obtained in the center part of the sample by TEM. The thickness of the layer is about 2.5 µm as estimated from Fig. 6. Fig. 7a shows a DF-TEM image obtained on the cross-section which was used for the determination of the grain size. Namely, the diameter of the bright spots was determined and taken as the size of grains building up the material. The grain size distribution obtained from the evaluation of one hundred grains is plotted in Fig. 7b. The grain size varied between 5 and 27 nm with an average value of about 12 nm. This value is slightly smaller than the crystallite size estimated from the FWHM of the first diffraction peak using the Scherrer method (about 20 nm, see above). This difference can be caused by the fact that beside the main fcc structure a minor phase also exists as suggested by the small XRD peak appeared at the right shoulder of the fcc 111 reflection (see Fig. 4b). This satellite peak is almost four times broader than peak 111; therefore, the size of crystallites out of the main fcc phase is surely much smaller than 20 nm (about 5 nm). The difference between the crystallite and grain sizes obtained by XRD and TEM, respectively, can also be attributed to the orders of magnitude larger volume studied by XRD (about 1 mm^3) as compared to that investigated TEM (about 1 µm^3). Fig. 7c reveals that the grains contain twin faults.

Fig. 7d shows an electron diffraction pattern obtained on the area shown in Fig. 7a. The rings are mainly related to an fcc phase as shown by the indices in the two-dimensional diffraction pattern, in accordance with the XRD results (see Fig. 4a). The integration of the intensity along the diffraction rings yielded the pattern shown in Fig. 7e. It can be seen that beside the main fcc peaks, reflections of a secondary bcc phase also appeared in the diffractogram. Fig. 7f shows the first part of the
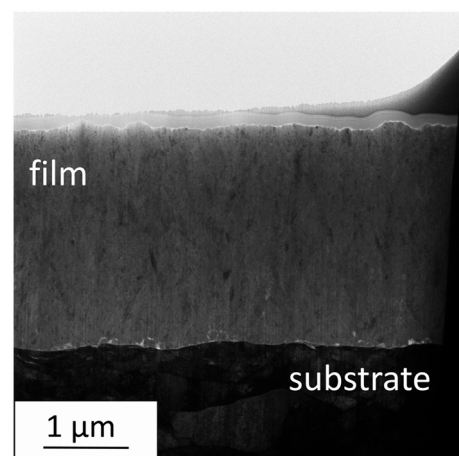

Fig. 5. Nelson-Riley plot for the determination of the lattice constant (*a*) of the main fcc phase.

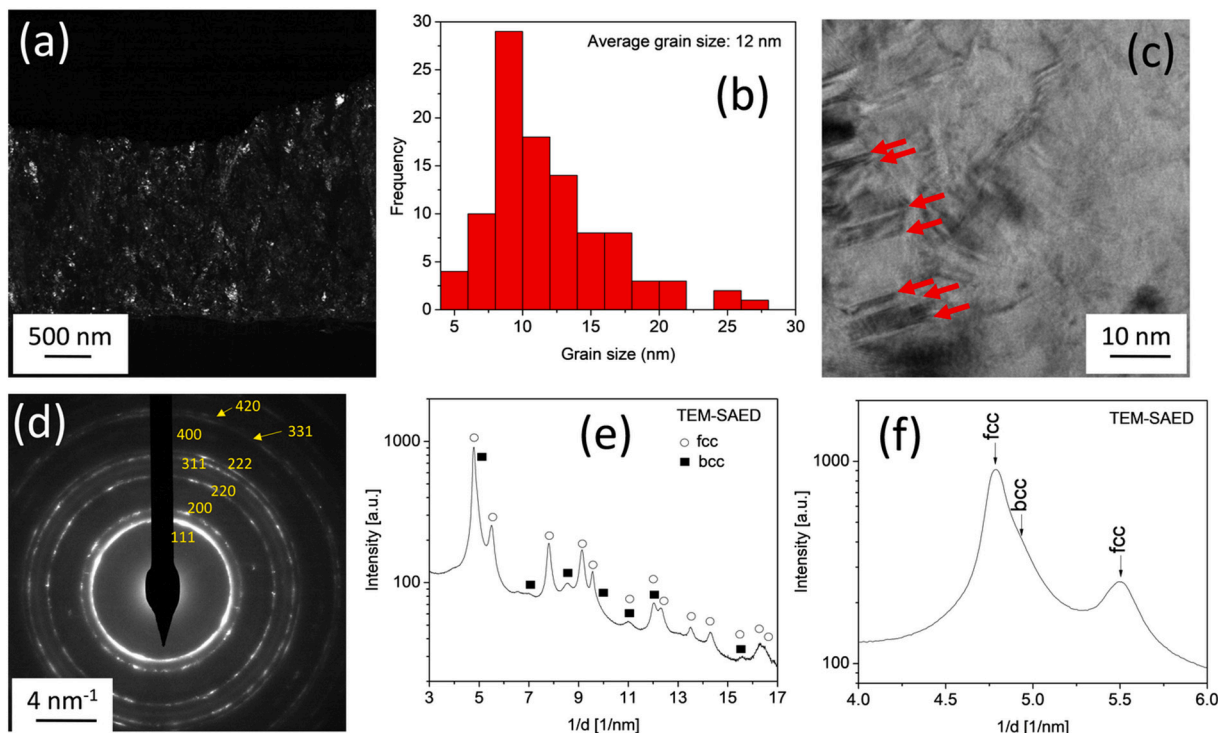**Fig. 6.** TEM cross-sectional view of the Co–Fe–Ni–Zn film.

Fig. 7. (a) TEM-DF image taken on the cross-section of the coating. (b) Grain size distribution determined from the evaluation of the TEM-DF image in (a). (c) TEM-BF micrograph showing nanotwins as indicated by red arrows. (d) Selected area diffraction pattern obtained on the part of the sample shown in panel (a). The indices of the fcc rings are indicated. The diffraction pattern obtained by the integration of the intensity along the diffraction rings is shown in (e). On the horizontal axis, *d* denotes the lattice spacing. The first part of the diffraction pattern with a higher magnification is presented in (f).

diffraction pattern with a higher magnification, revealing a shoulder at the right side of the main 111 fcc peak, similar to the XRD results (see Fig. 4b). Taking into account the other non-fcc peaks in the diffractogram, this peak at the shoulder corresponds to the 110 reflection of the secondary bcc phase. Other bcc peaks are not visible in the X-ray diffractogram as either they are very weak (such as the reflection at the *2θ* angle of 64.3°) or overlap with Ta peaks (such at that at 82.2°). Therefore, Nelson–Riley evaluation of lattice constant cannot be performed using the XRD data. The fraction of the bcc secondary phase was estimated from the integrated intensity ratio of the XRD bcc reflection 110 and the total area under the peaks related to the film. This fraction was found to be about 30 %. From the analysis of the position and the breadth of the bcc 110 peak which was separated from the fcc 111 reflection by fitting the XRD pattern (see Fig. 4b), the lattice constant and the crystallite size of the bcc phase were obtained as ~0.2895 nm and ~ 5 nm, respectively. It should be noted that the lattice constant

evaluated from the first peak can deviate significanty from the extrapolated value as shown in Fig. 4b, therefore the lattice constant was also evaluated from the TEM-SAED data using the Nelson–Riley method, and 0.287 ± 0.001 nm was obtained. This lattice parameter is close to the lattice constant value of Fe (0.2866 nm), the only constituent of the present MPEA forming bcc structure in pure form.

The BF-TEM image in Fig. 8a reveals that the microstructure consists of columns with the thickness of about 30 nm which are separated by bright boundaries (indicated by yellow arrows in the figure). The columns contain several grains; i.e., the grain size is smaller than the column width. The boundaries between the columnar structural features appear in dark contrast in the HAADF images (an example is shown in Fig. 8b). Additional HRTEM study revealed that these boundaries have an amorphous structure. An illustrative example for the HRTEM images is shown in Fig. 8c where the amorphous boundaries are indicated by yellow arrows. The thickness of these boundaries is about 2 nm. It is
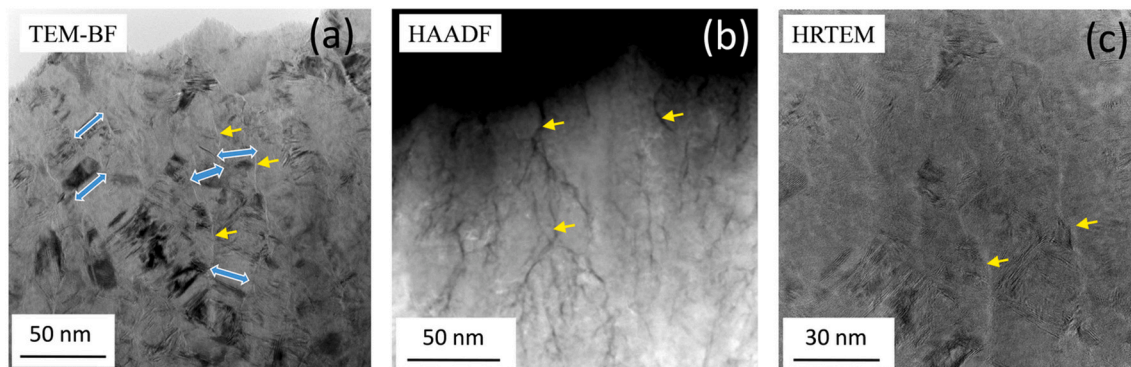

Fig. 8. (a) TEM-BF, (b) HAADF and (c) HRTEM images taken on the cross-section of the electrodeposited Co–Fe–Ni–Zn film. The yellow arrows indicate amorphous boundaries between polycrystalline columns. The blue double arrows show the width of these columns.

6

noted that although the TEM results shown in this study obtained on the top part of the film (i.e., near the solution side), very similar microstructure and chemical composition were detected in the bottom part of the layer (substrate side; not presented here).

The amorphous boundaries can be considered as another minor phase in addition to the bcc secondary phase. If we assume a model in which the crystalline columns having square cross-section and an edge dimension of 30 nm are covered by an amorphous layer with a thickness of 2 nm, an amorphous fraction of 12 % can be obtained. Fig. 9 shows that the amorphous boundaries are slightly enriched in Ni and depleted in Fe. Chemical compositional difference between the major fcc and the minor bcc phases may also exist. On the other hand, chemical inhomogeneity in the crystalline part of the layer was not observed by TEM which may be caused by the overlapping of grains within the FIB lamella; i.e., the chemical composition measured by TEM-EDS cannot be related to single grains.

3.3. Mechanical performance as determined by nanoindentation

Fig. 10a shows the nanohardness distribution measured on the Co—Fe—Ni—Zn MPEA film. The hardness values varied between 4.9 and 17.5 GPa. The average hardness was obtained as 9.2 GPa. The hardness distribution has a relatively long tail part at the higher values which may be caused by the variation of grain size, texture and the amount of the minority (bcc and amorphous) phases. A smaller grain size and a higher fraction of the minority phases locally may yield a higher nanohardness.

The elastic modulus histogram obtained by nanoindentation is shown in Fig. 10b. The average Young's modulus is 197 GPa. Although the elastic modulus distribution also has a long tail part at the high values, this effect is less pronounced compared to the hardness. This observation suggests that the hardness is more sensitive to the structural variations in the present MPEA layer than the Young's modulus.

Former nanoindentation experiments performed on various MPEA thin films and bulk materials yielded hardness values between 3.6 and 15 GPa as shown in Table 3 [56–58]. It should be noted that only those nanoindentation results were collected from the literature for which the applied load was similar or not significantly higher than that used in the present study (10 mN). This condition must be fulfilled if we wanted to avoid the indentation size effect (ISE) in the comparison of the hardness values. Due to ISE, the measured nanohardness may increase with decreasing the applied load. A former study [59] has shown that at the above load of 10 mN the ISE is marginal; i.e., the nanohardness values measured on different MPEA compositions and listed in Table 3 can be compared.

Table 3 shows that very high hardness values (12–15 GPa) were observed for FeCrSiNb and FeMnNiAl MPEAs processed by ion beam sputtering [14,60]. For the FeCrSiNb sample, the extreme hardness values were explained by the amorphous structure of the material which is hard to deform [14]. In the case of the FeMnNiAl MPEA, the material was a nanocrystalline body-centered cubic (bcc) structure with the crystallite size of 5–10 nm. In this case, both the extremely fine structure and the basically hard bcc structure can explain the very high hardness. The other MPEAs in Table 3 have fcc structure similar to our electrodeposited CoFeNiZn MPEA. They have lower average hardness (between 3.6 and 6.9 GPa) than that for the electroplated CoFeNiZn layer (9.2 GPa). This superior hardness can be attributed to the very small average grain size (~12 nm as determined by TEM), and the strengthening effect of the bcc and amorphous minority phases formed during deposition. Therefore, the present study demonstrated that electroplating is capable of producing fcc MPEA coatings with a similar or higher hardness as other layer deposition techniques.

It should also be noted that there is at least one advantage of the present Co-Fe-Ni-Zn MPEA layer compared to the common fcc alloy films such as Ni and its alloys (e.g., Ni—Mo, Ni—Fe and Ni—W): the considerably higher hardness. For Ni and its conventional alloys processed by electrodeposition, the hardness was not higher than 7 GPa even if they exhibited a nanostructure [61] while for the present MPEA composition an average hardness of 9.2 GPa was achieved. It should be noted that the Co—Fe—Ni—Zn MPEA layer produced in this paper is a novel composition; therefore, beside the high hardness other beneficial properties may be explored in the future.

4. Conclusions

A 2.5 μm thick Co—Fe—Ni—Zn MPEA film was successfully deposited on a Ta substrate by electroplating. The component distribution, the microstructure and the mechanical performance of the coating were studied and the following conclusions were drawn:

1. The composition of the layer obtained by electroplating was 32 % Co, 27 % Fe, 21 % Ni and 20 % Zn (at.%) as determined by SEM-EDS. Due to the optimized cell geometry, the composition was laterally even, with ±1 % random fluctuation within 85 % of the radius of the plated disc. As a result of the application of pulse plating, no in-depth composition variation occurred either, as revealed by TEM.

2. The film has a main fcc phase with the lattice constant of about 0.3620 nm. The average grain size was as small as ~12 nm. The size distribution was wide spanning from 5 to 27 nm. The microstructure also contains a bcc minority phase and ~ 2 nm thick amorphous boundaries separating polycrystalline columns. This amorphous phase is enriched in Ni and depleted in Fe. XRD suggests that the bcc
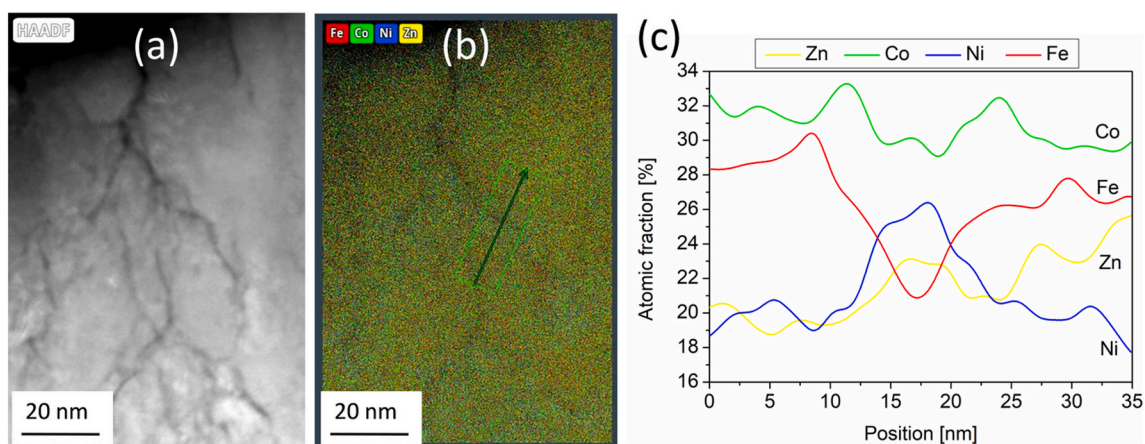

Fig. 9. (a) HAADF image and (b) STEM-EDS elemental maps and (c) a line profile taken across an amorphous boundary. Spatial distribution of the four elements along the line indicate that the boundary is enriched in Ni and depleted in Fe.
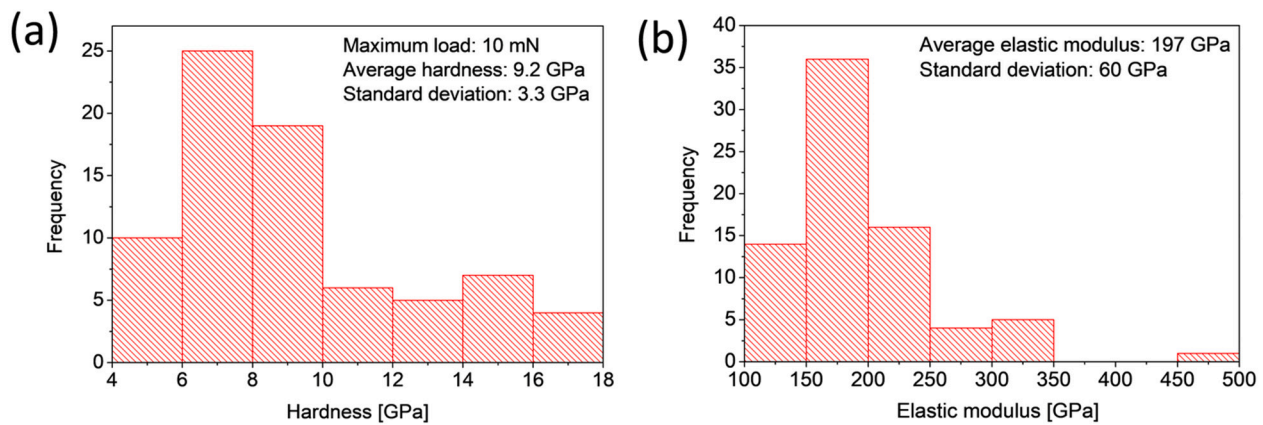
Fig. 10. Histograms showing the distributions of the hardness (a) and the elastic modulus (b) as determined by nanoindentation.

Table 3

Hardness values of MPEAs collected from the literature and studied in the present work. The composition and the processing route of MPEAs, as well as the load applied in nanoindentation are also shown. "a" denotes amorphous materials.

Composition	Method of manufacturing	Load (mN)	Hardness (GPa)	Reference
FeCrSiNb (a)	Ion beam sputtering	50	15.0 ± 1.2	[14]
CoCrFeNi (fcc)	Vacuum induction melting	100	6.9	[49]
FeMnNiAl (bcc)	Ion beam sputtering	10	11.7 ± 0.7	[57]
CoCrFeMnNi (fcc)	Cold spray	20	4.2	[54]
CoCrFeNi (fcc)	Arc melting	100	3.6	[55]
CoFeNiZn (fcc)	Electrodeposition	10	9.2	Present study

minority phase has a smaller crystallite size compared to the main fcc structure.

3. The average hardness and elastic modulus determined by nano-indentation were 9.2 and 197 GPa, respectively. This hardness is much higher than the values reported formerly on fcc MPEAs processed by other methods (3.6–6.9 GPa) which can be explained by the very small grain size and the existence of the bcc and amorphous minority phases.

4. The present study demonstrates the potential of electroplating in producing hard MPEA coatings. While the present work refers to a specific quaternary alloy of near-even molar fractions, the tuning of the solution composition and the electrical parameters of the deposition can be used to screen the impact of the compositon on the microstructure and the hardness of the resulting layer.

CRediT authorship contribution statement

Péter Nagy: Data curation, Formal analysis, Methodology, Investigation, Writing – original draft, Visualization. **László Péter:** Conceptualization, Methodology, Investigation, Supervision, Writing – original draft. **Zsolt Czigány:** Data curation, Investigation, Visualization, Writing – review & editing. **Nguyen Quang Chinh:** Formal analysis, Investigation, Writing – review & editing. **Jenő Gubicza:** Conceptualization, Supervision, Visualization, Writing – original draft.

Declaration of competing interest

The authors declare that they have no known competing financial interests or personal relationships that could have appeared to influence the work reported in this paper.

References

[1] B. Cantor, I.T.H. Chang, P. Knight, A.J.B. Vincent, Microstructural development in equiatomic multicomponent alloys, Mater. Sci. Eng. A (2004) 375–377, https://doi.org/10.1016/j.msea.2003.10.257.

[2] J.W. Yeh, S.K. Chen, S.J. Lin, J.Y. Gan, T.S. Chin, T.T. Shun, C.H. Tsau, S.Y. Chang, Nanostructured high-entropy alloys with multiple principal elements: novel alloy design concepts and outcomes, Adv. Eng. Mater. 6 (2004) 299–303, https://doi.org/10.1002/adem.200300567.

[3] J.W. Yeh, Alloy design strategies and future trends in high-entropy alloys, JOM. 65 (2013) 1759–1771, https://doi.org/10.1007/s11837-013-0761-6.

[4] Z.S. Nong, Y.N. Lei, J.C. Zhu, Wear and oxidation resistances of AlCrFeNiTi-based high entropy alloys, Intermetallics. 101 (2018) 144–151, https://doi.org/10.1016/J.INTERMET.2018.07.017.

[5] P.T. Hung, M. Kawasaki, J.K. Han, J.L. Lábár, J. Gubicza, Microstructure evolution in a nanocrystalline CoCrFeNi multi-principal element alloy during annealing, Mater. Charact. 171 (2021), 110807, https://doi.org/10.1016/j.matchar.2020.110807.

[6] W. Li, P. Liu, P.K. Liaw, Microstructures and properties of high-entropy alloy films and coatings: a review, Mater. Res. Lett. 6 (2018) 199–229, https://doi.org/10.1080/21663831.2018.1434248.

[7] M. Traversier, P. Mestre-Rinn, N. Peillon, E. Rigal, X. Boulnat, F. Tancret, J. Dhers, A. Fraczkiewicz, Nitrogen-induced hardening in an austenitic CrFeMnNi high-entropy alloy (HEA), Mater. Sci. Eng. A 804 (2021), 140725, https://doi.org/10.1016/J.MSEA.2020.140725.

[8] X. Zhong, Q. Zhang, J. Xie, M. Wu, F. Jiang, Y. Yan, Z. Wang, Mechanical properties and microstructure of the Al0.3CoCrFeNiTi0.3 high entropy alloy under dynamic compression, Mater. Sci. Eng. A 812 (2021), 141147, https://doi.org/10.1016/J.MSEA.2021.141147.

[9] J. Gao, Y. Jin, Y. Fan, D. Xu, L. Meng, C. Wang, Y. Yu, D. Zhang, F. Wang, Fabricating antibacterial CoCrCuFeNi high-entropy alloy via selective laser melting and in-situ alloying, J. Mater. Sci. Technol. 102 (2022) 159–165, https://doi.org/10.1016/J.JMST.2021.07.002.

[10] N. Hua, W. Wang, Q. Wang, Y. Ye, S. Lin, L. Zhang, Q. Guo, J. Brechtl, P.K. Liaw, Mechanical, corrosion, and wear properties of biomedical Ti–Zr–Nb–ta–Mo high entropy alloys, J. Alloys Compd. 861 (2021), 157997, https://doi.org/10.1016/J.JALLCOM.2020.157997.

[11] X. Hu, X. Liu, D. Yan, Z. Li, A high-density non-equiatomic WTaMoNbV high-entropy alloy: alloying behavior, microstructure and mechanical properties, J. Alloys Compd. 894 (2022), 162505, https://doi.org/10.1016/J.JALLCOM.2021.162505.

[12] B. Liu, J. Wu, Y. Cui, Q. Zhu, G. Xiao, S. Wu, G. han Cao, Z. Ren, Structural evolution and superconductivity tuned by valence electron concentration in the Nb-Mo-re-Ru-Rh high-entropy alloys, J. Mater. Sci. Technol. 85 (2021) 11–17, https://doi.org/10.1016/J.JMST.2021.02.002.

[13] Y. Zhang, M. Liu, J. Sun, G. Li, R. Zheng, W. Xiao, C. Ma, Excellent thermal stability and mechanical properties of bulk nanostructured FeCoNiCu high entropy alloy, Mater. Sci. Eng. A 835 (2022), 142670, https://doi.org/10.1016/J.MSEA.2022.142670.

[14] W. Muftah, J. Allport, V. Vishnyakov, Corrosion performance and mechanical properties of FeCrSiNb amorphous equiatomic HEA thin film, Surf. Coatings Technol. 422 (2021), 127486, https://doi.org/10.1016/J.SURFCOAT.2021.127486.

[15] M.C. Haciismailoglu, K. Sarlar, A. Tekgül, I. Kucuk, Thermally evaporated FeMGaMnSi (MCo, Ni) high entropy alloy thin films: magnetic and magnetoresistance properties, J. Non-Cryst. Solids 539 (2020), 120063, https://doi.org/10.1016/J.JNONCRYSOL.2020.120063.

[16] Y. Shi, B. Yang, P.D. Rack, S. Guo, P.K. Liaw, Y. Zhao, High-throughput synthesis and corrosion behavior of sputter-deposited nanocrystalline Alx(CoCrFeNi)100-x combinatorial high-entropy alloys, Mater. Des. 195 (2020), 109018, https://doi.org/10.1016/j.matdes.2020.109018.

[17] P. Nagy, N. Rohbeck, G. Roussely, P. Sortais, J.L. Lábár, J. Gubicza, J. Michler, L. Pethö, Processing and characterization of a multibeam sputtered nanocrystalline CoCrFeNi high-entropy alloy film, Surf. Coatings Technol. 386 (2020), 125465, https://doi.org/10.1016/j.surfcoat.2020.125465.

[18] P. Nagy, N. Rohbeck, Z. Hegedűs, J. Michler, L. Pethö, J.L. Lábár, J. Gubicza, Microstructure, hardness, and elastic Modulus of a multibeam-sputtered Nanocrystalline co-Cr-Fe-Ni compositional complex alloy film, Materials (Basel). 14 (2021) 3357, https://doi.org/10.3390/ma14123357.

[19] P. Nagy, N. Rohbeck, R.N. Widmer, Z. Hegedűs, J. Michler, L. Pethö, J.L. Lábár, J.Ő. Gubicza, Combinatorial Study of Phase Composition, Microstructure and Mechanical Behavior of Co-Cr-Fe-Ni Nanocrystalline Film Processed by Multiple-Beam-Sputtering Physical Vapor Deposition 2319, 2022, https://doi.org/10.3390/ma15062319.

[20] P. Nagy, B. Kaszás, I. Csabai, Z. Hegedűs, J. Michler, L. Pethö, J. Gubicza, Machine learning-based characterization of the nanostructure in a combinatorial co-Cr-Fe-Ni compositionally complex alloy film, Nanomaterials. 12 (2022) 4407, https://doi.org/10.3390/nano12244407.

[21] C.Z. Yao, P. Zhang, M. Liu, G.R. Li, J.Q. Ye, P. Liu, Y.X. Tong, Electrochemical preparation and magnetic study of bi-Fe-co-Ni-Mn high entropy alloy, Electrochim. Acta 53 (2008) 8359–8365, https://doi.org/10.1016/j.electacta.2008.06.036.

[22] C.Z. Yao, P. Zhang, Y.X. Tong, D.C. Xia, H.X. Ma, Electrochemical synthesis and magnetic studies of Ni-Fe-co-Mn-bi-tm high entropy alloy film, Chem. Res. Chinese Univ. 26 (2010) 640–644.

[23] C. Yao, B. Wei, P. Zhang, X. Lu, P. Liu, Y. Tong, Facile preparation and magnetic study of amorphous tm-Fe-co-Ni-Mn multicomponent alloy nanofilm, J. Rare Earths 29 (2011) 133–137, https://doi.org/10.1016/S1002-0721(10)60418-8.

[24] H. Li, H. Sun, C. Wang, B. Wei, C. Yao, Y. Tong, H. Ma, Controllable electrochemical synthesis and magnetic behaviors of mg-Mn-Fe-co-Ni-Gd alloy films, J. Alloys Compd. 598 (2014) 161–165, https://doi.org/10.1016/j.jallcom.2014.02.051.

[25] V. Soare, M. Burada, I. Constantin, D. Mitrică, V. Bədiliţə, A. Caragea, M. Tàrcolea, Electrochemical deposition and microstructural characterization of AlCrFeMnNi and AlCrCuFeMnNi high entropy alloy thin films, Appl. Surf. Sci. 358 (2015) 533–539, https://doi.org/10.1016/j.apsusc.2015.07.142.

[26] F. Yoosefan, A. Ashrafi, S.M. Monir vaghefi, I. Constantin, Synthesis of CoCrFeMnNi high entropy alloy thin films by pulse electrodeposition: part 1: effect of pulse electrodeposition parameters, Met. Mater. Int. 26 (2020) 1262–1269, https://doi.org/10.1007/s12540-019-00404-1.

[27] A.M.J. Popescu, F. Branzoi, I. Constantin, M. Anastasescu, M. Burada, D. Mitrică, I. Anasiei, M.T. Olaru, V. Constantin, Electrodeposition, characterization, and corrosion behavior of CoCrFeMnNi high-entropy alloy thin films, Coatings. 11 (2021) 1367, https://doi.org/10.3390/coatings11111367.

[28] F. Yoosefan, A. Ashrafi, S.M., Monir vaghefi, characterization of co–Cr–Fe–Mn–Ni high-entropy alloy thin films synthesized by pulse electrodeposition: part 2: effect of pulse electrodeposition parameters on the wettability and corrosion resistance, Met. Mater. Int. 27 (2021) 106–117, https://doi.org/10.1007/s12540-019-00584-w.

[29] J.C. Puippe, F. Leaman, Theory and Practice of Pulse Plating, American Electroplaters and Surface Finioshers Society, Orlando, Florida, USA, 1986.

[30] W.E.G. Hansal, S. Roy, P. Leisner, T. Green, A. Reichenbach, Pulse Plating, Eugen G Leuze Verlag KG, 2012. https://strathprints.strath.ac.uk/54397/.

[31] X. Zheng, P. Zhang, S. Tao, L. Wang, S. Zhang, N. Pang, M. Pan, Fabrication and magnetic properties of novel rare-earth-free Fe-Mn-bi-P thin films by one-step electrodeposition, Thin Solid Films 638 (2017) 400–405, https://doi.org/10.1016/J.TSF.2017.07.029.

[32] A. Aliyu, M.Y. Rekha, C. Srivastava, Microstructure-electrochemical property correlation in electrodeposited CuFeNiCoCr high-entropy alloy-graphene oxide composite coatings, Philos. Mag. 99 (2019) 718–735, https://doi.org/10.1080/14786435.2018.1554915.

[33] C.L.P. Pavithra, R.K.S.K. Janardhana, K.M. Reddy, C. Murapaka, J. Joardar, B. V. Sarada, R.R. Tamboli, Y. Hu, Y. Zhang, X. Wang, S.R. Dey, An advancement in the synthesis of unique soft magnetic CoCuFeNiZn high entropy alloy thin films, Sci. Rep. 11 (2021) 8836, https://doi.org/10.1038/s41598-021-87786-8.

[34] Z. Rong, C. Wang, Y. Wang, M. Dong, Y. You, J. Wang, H. Liu, J. Liu, Y. Wang, Z. Zhu, Microstructure and properties of FeCoNiCrX (XMn, Al) high-entropy alloy coatings, J. Alloys Compd. 921 (2022), 166061, https://doi.org/10.1016/J.JALLCOM.2022.166061.

[35] D. Ahmadkhaniha, J. Kruemmling, C. Zanella, Electrodeposition of high entropy alloy of Ni-Co-Cu-Mo-W from an aqueous bath, J. Electrochem. Soc. 169 (2022) 82515, https://doi.org/10.1149/1945-7111/ac87d5.

[36] C.L.P. Pavithra, R.K. Siri Kiran Janardhana, K. Madhav Reddy, C. Murapaka, X. Wang, S.R. Dey, One-dimensional co–cu–Fe–Ni–Zn high entropy alloy nanostructures, Mater. Res. Lett. 9 (2021) 285–290, https://doi.org/10.1080/21663831.2021.1896588.

[37] J. Sure, D.S.M. Vishnu, C. Schwandt, Direct electrochemical synthesis of high-entropy alloys from metal oxides, Appl. Mater. Today 9 (2017) 111–121, https://doi.org/10.1016/j.apmt.2017.05.009.

[38] B. Wang, J. Huang, J. Fan, Y. Dou, H. Zhu, D. Wang, Preparation of FeCoNiCrMn high entropy alloy by electrochemical reduction of solid oxides in molten salt and its corrosion behavior in aqueous solution, J. Electrochem. Soc. 164 (2017) E575–E579, https://doi.org/10.1149/2.1521714jes.

[39] H. Jiao, M. Wang, J. Tu, S. Jiao, Production of AlCrNbTaTi high entropy alloy via electro-Deoxidation of metal oxides, J. Electrochem. Soc. 165 (2018) D574–D579, https://doi.org/10.1149/2.0021813jes.

[40] J. Sure, D. Sri Maha Vishnu, C. Schwandt, Electrochemical conversion of oxide spinels into high-entropy alloy, J. Alloys Compd. 776 (2019) 133–141, https://doi.org/10.1016/j.jallcom.2018.10.171.

[41] J. Sure, D. Sri Maha Vishnu, C. Schwandt, Preparation of refractory high-entropy alloys by electro-deoxidation and the effect of heat treatment on microstructure and hardness, JOM. 72 (2020) 3895–3905, https://doi.org/10.1007/s11837-020-04367-2.

[42] J. Huang, K. Du, P. Wang, H. Yin, D. Wang, Electrochemical preparation and homogenization of face-centered FeCoNiCu medium entropy alloy electrodes enabling oxygen evolution reactions, Electrochim. Acta 378 (2021), 138142, https://doi.org/10.1016/j.electacta.2021.138142.

[43] Y. Yang, X. Luo, T. Ma, L. Wen, L. Hu, M. Hu, Effect of Al on characterization and properties of AlxCoCrFeNi high entropy alloy prepared via electro-deoxidation of the metal oxides and vacuum hot pressing sintering process, J. Alloys Compd. 864 (2021), 158717, https://doi.org/10.1016/j.jallcom.2021.158717.

[44] A. Csik, K. Vad, E. Tóth-Kádár, L. Péter, Spontaneous near-substrate composition modulation in electrodeposited Fe-co-Ni alloys, Electrochem. Commun. 11 (2009) 1289–1291, https://doi.org/10.1016/j.elecom.2009.04.027.

[45] L. Péter, A. Csik, K. Vad, E. Tóth-Kádár, Á. Pekker, G. Molnár, On the composition depth profile of electrodeposited Fe–co–Ni alloys, Electrochim. Acta 55 (2010) 4734–4741, https://doi.org/10.1016/j.electacta.2010.03.075.

[46] L. Péter, K.Z. Rozman, S. Sturm, Structure and composition of electrodeposited Fe-co-Ni alloys studied by transmission Electron microscopy, J. Electrochem. Soc. 165 (2018) D384–D392, https://doi.org/10.1149/2.0821809jes.

[47] K. Neuróhr, A. Csik, K. Vad, G. Molnár, I. Bakonyi, L. Péter, Near-substrate composition depth profile of direct current-plated and pulse-plated Fe–Ni alloys, Electrochim. Acta 103 (2013) 179–187, https://doi.org/10.1016/J.ELECTACTA.2013.04.063.

[48] L. Péter, K. Vad, A. Csik, R. Muñíz, L. Lobo, R. Pereiro, S. Šturm, K.Ž. Rožman, G. Molnár, K. Németh, K. Neuróhr, K. Boros, L. Pogány, I. Bakonyi, In-depth component distribution in electrodeposited alloys and multilayers, J. Electrochem. Sci. Eng. 8 (2018) 49–71, https://doi.org/10.5599/jese.480.

[49] W.C. Oliver, G.M. Pharr, An improved technique for determining hardness and elastic modulus using load and displacement sensing indentation experiments, J. Mater. Res. 7 (1992) 1564–1583, https://doi.org/10.1557/jmr.1992.1564.

[50] A. Brenner, Electrodeposition of Alloys, Academic Press, Now York and London, 1963.

[51] N. Zech, E.J. Podlaha, D. Landolt, Anomalous Codeposition of Iron group metals: I. experimental results, J. Electrochem. Soc. 146 (1999) 2886–2891, https://doi.org/10.1149/1.1392024.

[52] D. Landolt, Fundamental aspects of alloy plating, Plat. Surf. Finish. 88 (2001) 70–79.

[53] N. Eliaz, K. Venkatakrishna, A.C. Hegde, Electroplating and characterization of Zn-Ni, Zn-Co and Zn-Ni-Co alloys, Surf. Coatings Technol. 205 (2010) 1969–1978, https://doi.org/10.1016/j.surfcoat.2010.08.077.

[54] J.B. Nelson, D.P. Riley, An experimental investigation of extrapolation methods in the derivation of accurate unit-cell dimensions of crystals, Proc. Phys. Soc. 57 (1945) 160–177, https://doi.org/10.1088/0959-5309/57/3/302.

[55] J. Gubicza, X-Ray Line Profile Analysis in Materials Science, Hershey, USA, IGI Global, 2014.

[56] Y. Zhao, X. Wang, T. Cao, J.K. Han, M. Kawasaki, J. il Jang, H.N. Han, U. Ramamurty, L. Wang, Y. Xue, Effect of grain size on the strain rate sensitivity of CoCrFeNi high-entropy alloy, Mater. Sci. Eng. A 782 (2020), 139281, https://doi.org/10.1016/j.msea.2020.139281.

[57] M. Hussien, V. Vishnyakov, Single-phase FeMnNiAl compositionally complex alloy, J. Alloys Compd. 867 (2021), 158861, https://doi.org/10.1016/J.JALLCOM.2021.158861.

[58] J.E. Ahn, Y.K. Kim, S.H. Yoon, K.A. Lee, Tuning the microstructure and mechanical properties of cold sprayed Equiatomic CoCrFeMnNi high entropy alloy coating layer, Met. Mater. Int. 27 (2021) 2406–2415, https://doi.org/10.1007/s12540-020-00886-4.

[59] Z. Gao, Y. Zhao, J.M. Park, A.H. Jeon, K. Murakami, S. ichi Komazaki, K. Tsuchiya, U. Ramamurty, J. il Jang, Decoupling the roles of constituent phases in strengthening of hydrogenated nanocrystalline dual-phase high-entropy alloys, Scr. Mater. 210 (2022), 114472, https://doi.org/10.1016/J.SCRIPTAMAT.2021.114472.

[60] W. Huo, H. Zhou, F. Fang, X. Hu, Z. Xie, J. Jiang, Strain-rate effect upon the tensile behavior of CoCrFeNi high-entropy alloys, Mater. Sci. Eng. A 689 (2017) 366–369, https://doi.org/10.1016/j.msea.2017.02.077.

[61] J. Gubicza, Annealing-induced hardening in ultrafine-grained and nanocrystalline materials, Adv. Eng. Mater. 22 (2020) 1900507, https://doi.org/10.1002/adem.201900507.